Chemical Science

ROYAL SOCIETY OF CHEMISTRY

EDGE ARTICLE

View Article Online
View Journal | View Issue

Cite this: *Chem. Sci.*, 2025, **16**, 5007

All publication charges for this article have been paid for by the Royal Society of Chemistry

Insights into facile methane activation by a spin forbidden reaction with Ta^+ ions in the gas phase†

Yang Liu, [a] Milan Ončák, [*b] Tucker W. R. Lewis, [c] Marcel Meta, [d] Shaun G. Ard, [c] Nicholas S. Shuman, [*c] Jennifer Meyer, [d] Albert A. Viggiano [c] and Hua Guo [*a]

The activation of methane (CH_4) by transition-metal cations in the gas phase provides a model for understanding the impact of electronic spin on reactivity, with implications in single atom catalysis. In this work, we present a mixed quantum-classical trajectory surface hopping study on the nominally spin-forbidden reaction $Ta^+ + CH_4 \rightarrow TaCH_2^+ + H_2$. To facilitate the dynamics calculations, full twelve-dimensional PESs for three low-lying spin (quintet, triplet, and singlet) states are constructed using a machine learning method from density functional theory data. Furthermore, we report the temperature dependence of the rate coefficients for the $Ta^+ + CH_4 \rightarrow TaCH_2^+ + H_2$ reaction measured using the selected ion flow tube (SIFT) technique. The measured rate coefficient has a near zero temperature dependence and is approximately 50% of the capture limit at room temperature. Our theoretical results with a Gaussian-binning treatment of the product zero-point energy reproduced the experimental rate coefficient and the temperature dependence. Satisfactory agreement is also obtained between theory and differential cross sections measured recently using molecular beams combined with velocity map imaging. Specifically, our multi-state calculations confirm the indirect mechanism of this reaction with long-lived reaction intermediate after passing through the initial barrier and reveal that the kinetic bottleneck in this reaction is intersystem crossing between the quintet and triplet states. Furthermore, the energy disposal in the $TaCH_2^+$ (both singlet and triplet) and H_2 products is found to be largely statistical due to the long lifetime of the exit-channel complex.

Received 13th December 2024
Accepted 7th February 2025

DOI: 10.1039/d4sc08457h

rsc.li/chemical-science

Introduction

Methane (CH_4), the primary component of natural gas and methane clathrates, is a crucial hydrocarbon feedstock for fuel and chemical production. However, its low volumetric energy density results in high transportation and storage costs, limiting its use as a chemical energy source. The conversion of methane into value-added chemicals and fuels is critical not only for economic reasons but also for addressing environmental concerns related to greenhouse gas emissions. Consequently, significant research efforts have focused on converting methane into more energy-dense fuels or higher-value chemicals.[1,2] All these conversions begin with the activation of methane, which involves the weakening or breaking one of its four carbon–hydrogen bonds.[3] However, CH_4 is quite inert due to its strong C–H bonds, with a bond dissociation energy (BDE) of 4.5 eV.[4] In addition, methane has zero dipole moment and quadrupole moment, low polarizability (2.593 Å^3), and a high ionization energy of 12.6 eV.[5] These factors contribute to its low reactivity in chemical reactions, making catalysts essential for efficient chemical conversions. Common catalysts for methane activation are transition metals dispersed on oxide supports.[6–8] A major challenge in catalyst design is that nearly all newly formed bonds are weaker than the original C–H bond in methane. Therefore, highly active catalysts often lack selectivity. Recently, an increasing number of reports have suggested efficient methane activation with atomically dispersed transition metals.[9–11] These studies indicated that such single atom catalysis (SAC) sensitively depends on the immediate environment of the metal ion, which controls its partial charge and presumably spin.

A unique approach to understand the SAC is to investigate the activation of small molecules by transition metal ions in the gas phase.[12–14] For methane activation, it is known that many third-row transition metal cations (M^+) can readily

[a]*Department of Chemistry and Chemical Biology, Center for Computational Chemistry, University of New Mexico, Albuquerque, New Mexico 87131, USA. E-mail: hguo@unm.edu*

[b]*Universität Innsbruck, Institut für Ionenphysik und Angewandte Physik, Technikerstraße 25, 6020 Innsbruck, Austria*

[c]*Air Force Research Laboratory, Space Vehicles Directorate, Kirtland Air Force Base, New Mexico 87117, USA*

[d]*RPTU Kaiserslautern-Landau, Fachbereich Chemie and Forschungszentrum OPTIMAS, Erwin-Schrödinger Str. 52, 67663 Kaiserslautern, Germany*

† Electronic supplementary information (ESI) available. See DOI: https://doi.org/10.1039/d4sc08457h

dehydrogenate methane at room temperature to produce MCH_2^+,[15–31] which can then, *e.g.*, serve as an intermediate in the conversion of CH_4 to CH_2O. From a thermochemical perspective, the exothermic formation of $M{=}CH_2^+$ is viable only if the metal–methylidene bond strength $D_0(M{=}CH_2)$ is greater than the heat of dehydrogenation of methane, which is 4.743 ± 0.001 eV determined by the Active Thermochemical Tables (ATcT) approach.[22,32,33] Irikura and Beauchamp observed reactions between methane and Hf^+, Ta^+, W^+, Re^+, Os^+, Ir^+, Pt^+, and Au^+ and found that Ta^+, W^+, Os^+, Ir^+, and Pt^+ reacted at room temperature.[16] Later, Shayesteh *et al.* investigated the reactions of methane with 59 atomic metal cations at room temperature and found that the H_2 elimination channel occurred with As^+, Nb^+, Ta^+, W^+, Os^+, Ir^+, and Pt^+ ions.[29] In this work, we focus on the reaction of CH_4 activation by the open-shell transition-metal Ta^+ ions:

$$Ta^+ + CH_4 \rightarrow TaCH_2^+ + H_2 \quad (R1)$$

This reaction is highly efficient, with thermal rates comparable to gas kinetic.[29,30] However, as shown in Fig. 1, the reaction has a significant barrier and high endoergicity on the lowest quintet state (^{5}F). The facile reactivity can only be explained by efficient spin–orbit-mediated transitions from the high-spin quintet state to the low-spin triplet (and possibly singlet) excited state of the entrance channel, both of which have a submerged barrier. This so-called multi-state or two-state reactivity (TSR)[34–36] is a characteristic feature of many transition-metal-mediated processes where low-lying excited states play a crucial role.

Parke *et al.*[28] investigated (R1) using guided ion beam techniques. The observed decrease in the reaction cross section with increasing kinetic energy suggests that the reaction proceeds through an intermediate, offering valuable dynamic insights. Furthermore, supported by theoretical calculations, they concluded that the relatively low reaction efficiency (18–44%) is attributed to the spin-forbidden nature of the reaction. Very recently, Meta *et al.* investigated the dynamics of (R1) using crossed-beam velocity map imaging, providing detailed chemical dynamic information about (R1) for the first time.[37] The measured differential cross sections (DCSs) show that the product ions are dominated by isotropic scattering around the center-of-mass, indicating that the reaction is dominated by a complex-forming mechanism even at collision energies up to 1.3 eV. However, information about the identity of the long-lived complex and/or intermediate that governs this indirect mechanism is lacking. Little is known about the origin of the associated bottleneck that leads to this long lifetime. As shown in Fig. 1, the reaction begins on the quintet surface, forming a pre-reaction well (^{5}INT1) before the quintet saddle point (^{5}SP1). The formation of tantalum carbene ($Ta{=}CH_2^+$) in both the singlet and triplet product channels involves breaking two C–H bonds, forming two new bonds, and releasing molecular hydrogen. After crossing the triplet saddle point (^{3}SP1), the system undergoes a series of complex transformations to reach the product asymptotes. This mechanism is akin to a classic two-step process. First, oxidative addition occurs as the tantalum ion inserts into a C–H bond, followed by the migration of a second hydrogen atom to the metal center to form INT3. Then, reductive elimination of molecular hydrogen occurs from the metal center. Alternatively, the system can bypass INT3 *via* a four-centered transition state, SP4, to form INT5 and subsequently reach the products. The post-transition state well (INT2) following the first H-atom transfer may have a long lifetime

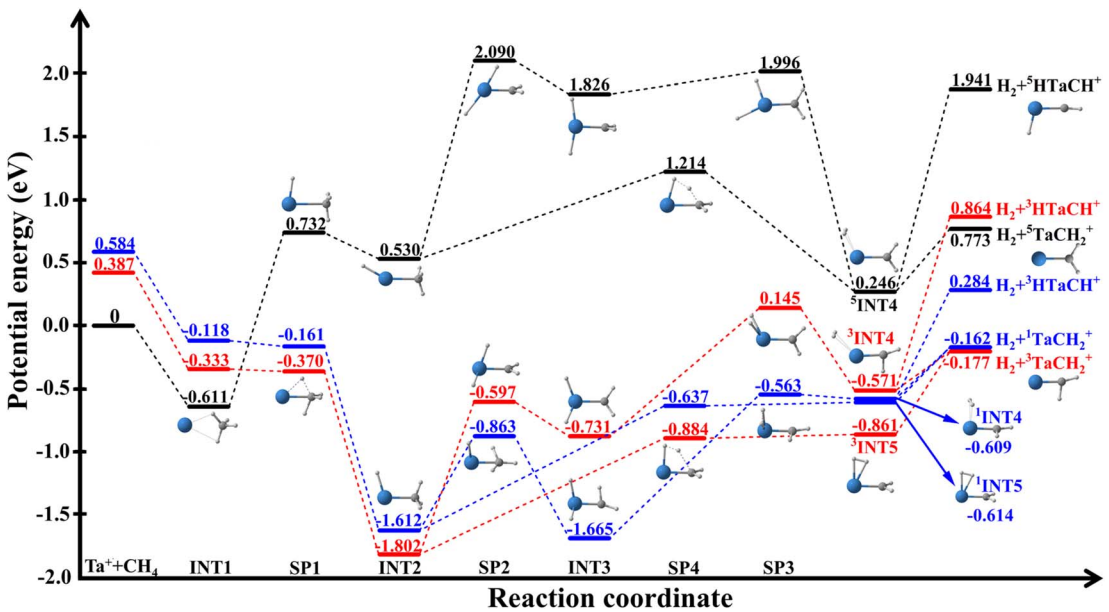

Fig. 1 Schematic of the $Ta^+ + CH_4 \rightarrow TaCH_2^+ + H_2$ reaction on the quintet, triplet, and singlet state surfaces (black, red, and blue, respectively). The energies with ZPE correction are calculated at the B3LYP/DZ level. The ZPE correction induces the energy of some saddle points to fall below the local minima.

because it must overcome a relatively large barrier (SP2 or SP4) associated with significant molecular rearrangement to other wells (INT3, INT4 and INT5), before forming the products. Since the collision energy in the crossed beam experiment allow the access to these wells, energy partition in the products sheds light on the molecular rearrangements in these reaction intermediates. To understand the microscopic mechanism and dynamics of such a complex reactive system, dynamical simulations are essential to determine whether the indirect mechanism is associated with the reactant complex $[Ta(CH_4)]^+$ (INT1), one of the intermediate complexes $[HTaCH_3]^+$ (INT2) and $[H_2TaCH_2]^+$ (INT3), or the product complex $[(H_2)TaCH_2]^+$ (INT4 and INT5).

The molecular beam experiment also measured the product kinetic energy distributions, revealing low kinetic energy for the products, which indicates that the products' internal degrees of freedom (DOFs) are highly excited. However, it remains unclear which product(s) ($TaCH_2^+$ and/or H_2) and which DOF(s) (vibration and/or rotation) are excited. It is also uncertain whether the reactivity of the reaction is governed by intersystem crossing (ISC) between the quintet and triplet states or by ^{3}SP1. Furthermore, the contribution of the singlet state to the reaction is unknown and cannot be easily determined experimentally due to instrumental limitations.

To address these mechanistic questions, we present here a comprehensive kinetic and dynamic study of this reaction, which is made possible by full-dimensional potential energy surfaces (PESs) of the quintet, triplet, and singlet states, based on approximately 64 300 density functional theory (DFT) points. The particular density functional used in these calculations has been benchmarked with high-level *ab initio* methods. The dynamic calculations were performed using the mixed quantum-classical trajectory surface hopping method, along with *ab initio* spin–orbit couplings determined from multireference configuration interaction (MRCI) calculations. This strategy has been used by us previously to study $Ta^+ + CO_2$ and $Nb^+ + CO_2$ reactions with much success.[38,39] A similar dynamical study has also been reported for the $FeO^+ + H_2$ reaction, which also proceeds through a TSR mechanism.[40] In addition, we remeasured thermal rate coefficients using a selected ion flow tube (SIFT) across a much wider temperature range than reported to date.

Results and discussion

Electronic structure calculations

The reaction pathways for the quintet, triplet, and singlet states are shown in Fig. 1, and the corresponding zero-point energy (ZPE)-corrected energies and frequencies of all stationary points calculated at the B3LYP/DZ level listed in Table S1.† The recent higher-level calculations at the CCSD(T)//B3LYP level[37] and available experimental values[5] are also included for comparison. The optimized geometries for the quintet, triplet, and singlet states are presented in Fig. S1–S3,† respectively. The B3LYP/DZ method provides very similar predictions to the CCSD(T)//B3LYP calculations, showing reasonable agreement within about 0.3 eV, except for the energy of the singlet $Ta^+ + CH_4$ asymptote. At the B3LYP/DZ level, the energy (0.584 eV) is significantly lower than the value calculated at the CCSD(T)//B3LYP level (1.328 eV)[37] and the experimental measurement (1.216 eV).[5] The underestimate for the singlet $Ta^+ + CH_4$ asymptote might be from the mis-convergence in the DFT calculations due to the multireference character. However, we believe this discrepancy has very limited impacts on our dynamic results due to the high energy of this channel, similar to the $Ta^+/Nb^+ + CO_2$ systems.[38,39]

As depicted in Fig. 1, the reaction between quintet Ta^+ ion ($^5Ta^+$) and CH_4 proceeds through a pre-reaction well (^{5}INT1, −0.611 eV) and must circumvent a very high barrier (^{5}SP1, 0.732 eV). INT1 is a complex formed due largely to electrostatic interaction, as evidenced by the comparable well depth in different spin states. The barrier features the insertion of the metal into a C–H bond. The product asymptotes are also very high, making the reaction an endoergic process. Hence, this adiabatic pathway is expected to be viable only at very high temperatures.

Alternatively, the reaction can also advance nonadiabatically *via* efficient ISC from the quintet to the triplet state, where ^{3}SP1 is submerged. After crossing ^{3}SP1, the reaction enters a very deep well (^{3}INT2, −1.802 eV), which is formed by an oxidative addition reaction in which the tantalum ion inserts into a C–H bond, causing the hydrogen atom to migrate from the carbon to the tantalum atom. Starting from ^{3}INT2, there are two ways to reach the products: one is ^{3}INT2 → ^{3}SP2 → ^{3}INT3 → ^{3}SP3 → ^{3}INT4 → products, and the other is ^{3}INT2 → ^{3}SP4 → ^{3}INT5 → products. In both reaction paths, the formation of the products is up-hill. Similar reaction paths can also be found on the singlet state surface.

The adiabatic reaction channel in the quintet state is endothermic, with a reaction energy of 0.773 eV at the B3LYP/DZ level. In contrast, the nonadiabatic reaction channel is slightly exothermic in the triplet and singlet states, with reaction energies of −0.177 eV and −0.162 eV, respectively, at the B3LYP/DZ level, they are close to the values at the CCSD(T)//B3LYP level (−0.297 and −0.302 eV).[37] The reaction energy of the triplet state at the B3LYP/DZ level also agrees reasonably well with the experimental measurement of -0.10 ± 0.02 eV by Armentrout and coworkers.[28] Independently, the $TaCH_2^+$ photodissociation experiment of Metz and coworkers[18] sets a lower bound on the exothermicity of the reaction at −0.23 eV, which is consistent with our values.

We further note that all PESs leads also to the $HTaCH^+ + H_2$ products, as shown in Fig. 1. Due to the high energies, however, the $H_2 + HTaCH^+$ asymptote represents only a minor channel, and will not be discussed further.

Potential energy surfaces

About 64 300 quintet, triplet, and singlet energies were calculated at the level of B3LYP/DZ level and represented using the permutation-invariant-polynomial neural-network (PIP-NN) method to generate the corresponding spin-specific twelve-dimensional PESs. For the quintet, triplet, and singlet PESs, the final root mean square errors (RMSEs) are 33.8, 41.5, and

40.4 meV, respectively, and the maximum errors are 573.0, 737.9, and 501.1 meV. A graphical representation of the errors throughout the entire energy range up to 7 eV is shown in Fig. S4a and S4b.† The majority of points have a fitting error under 20 meV. The energies, geometries, and harmonic frequencies of the stationary points obtained on the PESs can be found in Table S1 and Fig. S1–S3.† These static properties were well reproduced on the newly constructed PESs, except for the energy of ^{5}INT2, which differs by 0.213 eV between B3LYP/DZ and the PES. However, due to the high barrier associated with the quintet state, this channel is negligible and thus it will not affect the dynamic results. Fig. S5–S7† depict the potential energies along the minimum energy paths (MEPs) from SP1 to SP4 on the quintet, triplet, and singlet PESs, respectively.

Kinetics and mechanism

Fig. 2 illustrates the comparison of calculated rate coefficients with previous experimental data at room temperature[29,30] and the new ones measured using SIFT. The newly measured rate coefficient at room temperature (300 K) is in good agreement with previous results,[29,30] as shown in Fig. 2. The temperature dependence over this range is very mild, and the rate coefficients are at about 40% of the Langevin–Gioumousis–Stevenson capture limit. This weak temperature dependence is consistent with the energy dependence reported from a prior guided ion beam measurement[28] showing cross sections at low collision energies (E_c) at a constant fraction of the Langevin–Gioumousis–Stevenson value. Importantly, the facile reactivity is consistent with an exothermic reaction lacking an activation energy. However, the features of the PES responsible for reducing reactivity below the capture limit are not clear from experiment alone. The theoretical results (FSSH in the figure) are larger than the experiment, which is due to the fact that there are many trajectories with vibrational energy below the ZPE level of the H_2 product. Given the fact that the nonadiabatic reaction pathway is nearly thermoneutral and H_2 has a large vibrational frequency, it is not surprising that ZPE violation is quite acute in this system. To mitigate this problem, the one-dimensional Gaussian binning (1GB) method, an approach to address the ZPE leakage issue (see Methods for detail), was used. As shown in Fig. 2, the 1GB corrected rate coefficients (FSSH + 1GB) are in much better agreement with the experiment.

While the thermal rate coefficient of the $Ta^+ + CH_4 \rightarrow TaCH_2^+ + H_2$ reaction constitutes a large percentage of the capture limit, the differences indicate a kinetic bottleneck for the reaction, in agreement with the results from recent dynamics experiments. To determine whether the ISC from quintet to triplet states or the saddle points on the triplet state (^{3}SP1) is the controlling factor for this reaction, a critical point in any TSR system, we analysed the trajectories calculated at E_c = 0.7, 1.0, and 1.3 eV. The energies were chosen to allow for direct comparison with experiment. Fig. 3 show the distributions of the number of the transitions from quintet to triplet and from triplet to singlet for the three pathways: nonreactive (black), $^5Ta^+ + CH_4 \rightarrow {}^3TaCH_2^+ + H_2$ (red), and $^5Ta^+ + CH_4 \rightarrow {}^1TaCH_2^+ + H_2$ (blue). For nonreactive trajectories, only a tiny minority of trajectories, 1.7, 1.6, and 1.5% at E_c = 0.7, 1.0, and 1.3 eV, respectively, underwent a quintet → triplet → quintet transition. For most reactive trajectories, only a single transition from quintet to triplet is needed for the reaction to happen. In a small subset of trajectories, 2 to 10 transitions are required. The distribution of these transitions declined rapidly as the number of transitions increased. Consequently, from the above analysis, we can safely conclude that the ISC is the rate-limiting

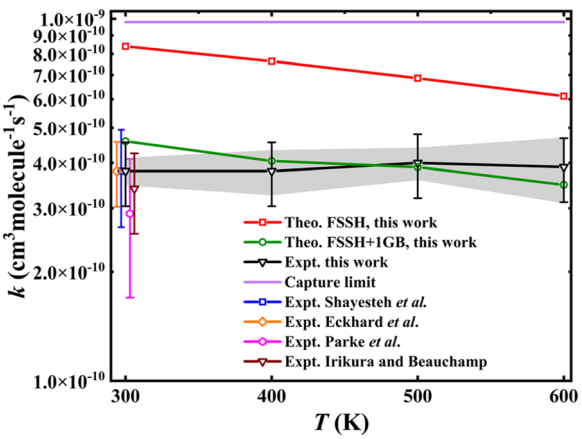

Fig. 2 Comparison of the calculated and experimentally measured rate coefficients[16,28–30] for the $Ta^+ + CH_4 \rightarrow TaCH_2^+ + H_2$ reaction. The error bars on the newly measured experimental rates indicate systematic uncertainties, while the shaded gray region denotes uncertainties for comparisons across different temperatures. The experimental rates from the literature, originally measured at 300 K, are slightly shifted to enhance clarity in the comparisons.

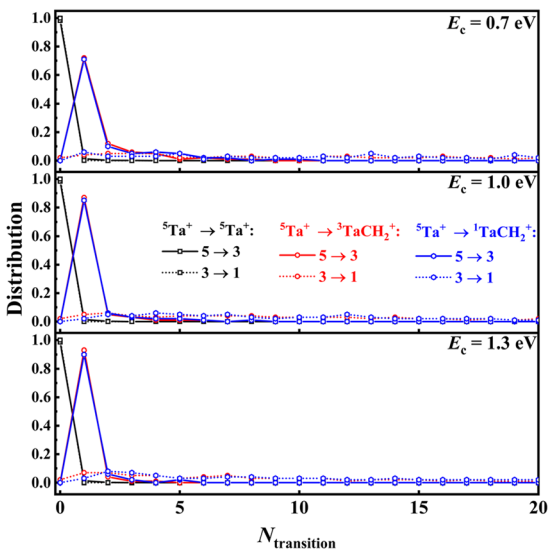

Fig. 3 Distributions of the number of ISC transitions from the quintet to triplet (solid line) and from the triplet to singlet (dotted line) for the nonreactive (black), $^5Ta^+ + CH_4 \rightarrow {}^3TaCH_2^+ + H_2$ (blue), and $^5Ta^+ + CH_4 \rightarrow {}^1TaCH_2^+ + H_2$ (red) reactions at three collision energies, respectively. Note that the reverse transitions from triplet to quintet (3 → 5) and from singlet to triplet (1 → 3) are necessary for the nonreactive channel (black lines).

step in this reaction. This reinforces the conclusion of Parke *et al.*[28] that the relatively low efficiency of the reaction is a result of its spin-forbidden nature, as discussed above. Fig. S8† shows a comparison of the geometries of ^{3}SP1 and the minimum energy crossing point (MECP) between the quintet and triplet states. As seen, the MECP is located before ^{3}SP1 but they have very similar structures. Furthermore, the energy of the MECP is −0.274 eV at the B3LYP/DZ level, which is slightly lower than that of ^{3}SP1 (−0.191 eV, without ZPE correction). This indicates that overcoming ^{3}SP1 is relatively easy for this reaction once the crossing occurs, suggesting that the energy barrier on the triplet state is not the kinetic bottleneck. In contrast, in the prototypical $FeO^+ + H_2$ reaction,[40] the energy of MECP is 0.351 eV lower than that of the saddle point, resulting in that the saddle point is the rate-limiting step rather than the spin-state change at low reaction energy.

Cross sections and product energy disposal

The velocity distributions of the product ion $TaCH_2^+$ are displayed in Fig. 4(a)–(c) for experimental data[37] and Fig. 4(d)–(f) for calculated data, at three collision energies. The superimposed circles represent the maximum possible energy partitioned into the product kinetic energy, starting from the quintet (green) and triplet (orange) reactants.[37] It is apparent that some of the experimental events fall outside the velocity space defined by the kinematic cut-off, indicating an overestimation of the kinetic energy of the product ion $TaCH_2^+$.

The calculated energy distributions of the internal energy align well with experimental measurements at the position of the peak and the right side of the peak. Nonetheless, the experimental distributions are broader than the theoretical ones. On the left side of the peak, and surprisingly, the experiments show some negative internal energy distributions which is due to E_{int} being calculated with respect to the kinematic cut-off. The experimental and theoretical internal energies of the products are obtained using the formula:

$$E_{int} = E_{rel} + E_{exo} - E'_{rel},$$

where E_{rel}, E_{exo}, and E'_{rel} represent the relative collision energy, reaction exothermicity, and the product relative translational energy, respectively. The negative contribution to E_{int} may result from missing contributions to the energy balance, such as electronically excited states of Ta^+ or the internal energy of CH_4, as discussed in ref. 37, which includes a detailed analysis on the experimental energy spread. The experimental and theoretical velocity distributions of the product ion $TaCH_2^+$ show predominantly isotropic scattering around the center of mass, but discrepancies exist between the two. The calculated and

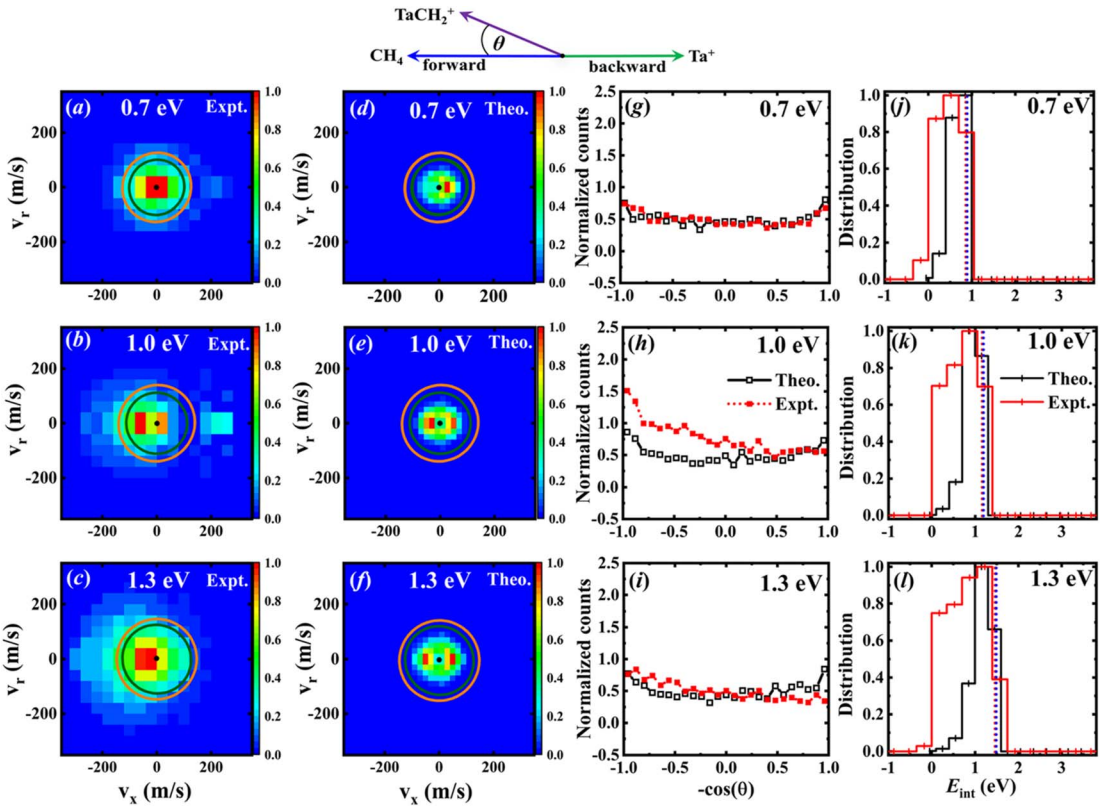

Fig. 4 (a)–(c) The experimental[37] velocity distributions of the $TaCH_2^+$ product ion at E_c = 0.7, 1.0, and 1.3 eV, respectively. (d–f) Similar to (a)–(c) but for the theoretical data. Histograms are normalized with the bin of highest intensity set to one. (g–i) The corresponding integrated angular distributions from simulations with the experimental data[37] included for comparison. The definition of the scattering angle is also illustrated by the simplified Newton diagram. All distributions normalized to an area of one. The dotted lines in j–l are the calculated available energies for the triplet (red) and singlet (blue) product channels (since these values are nearly identical, the lines overlap). Experimental distributions are truncated at the kinematic cut-off for better comparison.

measured DCSs at E_c = 0.7, 1.0, and 1.3 eV are given in Fig. 4(g)–(i) as a function of cos(θ). The calculated velocity distributions are forward-backward symmetric at all three collision energies and agree well with the experimental at E_c = 0.7 eV. However, at E_c = 1.0 and 1.3 eV, the experimental DCSs have a forward bias. The differences in the DCS at high collision energies are also present in the $Ta^+/Nb^+ + CO_2$ systems,[38,39] possible explanations include the presence of additional electronic states at high collision energies and the underestimation of DFT calculations for the singlet state reactant asymptote. The calculated energy distributions of the internal energy, shown in Fig. 4(j)–(l), agree well with the experimental measurements at the position of the peak, but the experimental distributions are broader than the theoretical ones on the left side of the peak.

The nearly isotropically scattered product ion $TaCH_2^+$ indicates that the reaction is dominated by a complex-forming mechanism, suggesting a relatively long lifetime of a reaction complex. To identify the long-lived complex/intermediate of this reaction, we calculated the lifetimes of the pre-reaction well and post-reaction well, based on the same criteria as in the $Ta^+ + CO_2$ system.[38] For INT1, the time is measured between when the Ta–C distance becomes less than 4.5 Å and when the system crosses SP1, defined as the Ta–C distance less than 2.4 Å. This indicates that the system enters the post-transition state well. The lifetime of the post-transition state wells ends when the center of mass (COM) distance between the products exceeds 4.5 Å. We define the system as entering INT2 when only one of the C–H distances becomes longer than 1.4 Å. Similarly, the system is considered to enter INT3 when two of the C–H distances exceed 1.4 Å, provided that the distance between two hydrogen atoms farthest from the carbon atom exceeds 1.1 Å. Finally, if the distance between the two hydrogen atoms decreases to less than 1.1 Å, the system is assumed to reach INT4 or INT5 (the two structures are indistinguishable in this work). The average lifetimes of pre-reaction well are 0.63, 0.27, and 0.13 ps at E_c = 0.7, 1.0 and 1.3 eV, respectively, while for post-reaction well, we found INT2 and INT3 both have much longer lifetimes. They are 8.21, 7.47, and 9.41 ps for INT2 and 6.37, 4.98, and 5.46 ps for INT3 at the three collision energies, respectively. The lifetime of INT4 (or/and INT5) is 0.32, 0.25, 0.23 ps at the three collision energies, respectively. This is quite different from those observed in the $Ta^+/Nb^+ + CO_2$ systems in which the pre-reaction well has the longer lifetimes.[38,39] The complex-forming mechanism can also be demonstrated by analysing the relationship between the scattering angle and the impact parameter, as shown in Fig. S9,† which reveals no correlation between these variables, indicating the presence of a long-lived intermediate. This intermediate contributes to the forward-backward symmetric scattering patterns observed in our theoretical results.

The calculated average energy partitioning of the two products as a function of collision energy is shown in Fig. 5(a). The highly excited product internal energy is consistent with the experimentally observed low kinetic energy. The results indicate that both the vibrational and rotational modes of $TaCH_2^+$ are highly excited, while that of the molecular hydrogen H_2 product is quite moderate. However, this picture is somewhat deceiving as the former has six vibrational modes and three rotational

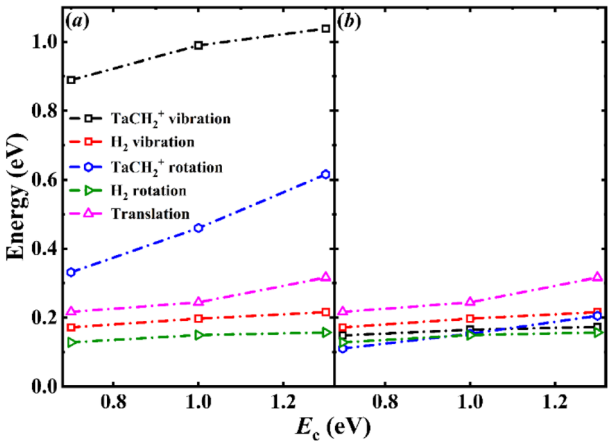

Fig. 5 (a) Product ($^{3,1}TaCH_2^+ + H_2$) energy partitioning to different product motion as a function of the collision energy. (b) The average energy partitioning per degree-of-freedom, namely, the average energy in each mode for the two products.

modes, rather than the single vibrational and two rotational modes for H_2. As illustrated in Fig. 5(b), the average amount of energy partitioned into the different types of motion divided by the number of associated degrees-of-freedom (DOFs) are quite comparable, suggesting equipartitioning of the available energy in product energy disposal. This is apparently a consequence of the long lifetime of the post-reaction well, where energy randomization must have taken place. The energy disposal in the title reaction is very different from that in the $Ta^+ + CO_2$ and $Nb^+ + CO_2$ reactions, where the energy disposal into the internal DOFs of MO^+ is dominant.[38,39] The long lifetime also results in a larger distribution of singlet state products for the reaction compared to the $Ta^+/Nb^+ + CO_2$ reactions because it increases the chance of crossing from triplet to singlet. Unlike the transitions from quintet to triplet, the distributions of transition numbers from the triplet to singlet state do not show a sharp peak but instead display a uniform distribution across the transition numbers, see Fig. 3. This is different from what we observed in the $Ta^+/Nb^+ + CO_2$ systems. The product branching is approximately 0.7/0.3 for $^3TaCH_2^+/^1TaCH_2^+$ at the three collision energies, whereas in the $Ta^+/Nb^+ + CO_2$ reactions, it is only about 0.9/0.1 for $^3TaO^+/^1TaO^+$ and $^3NbO^+/^1NbO^+$.[38,39]

Fig. S10(a) and (b)† show the experimental[37] and theoretical velocity distribution of $TaCD_2^+$, respectively, at the E_c = 1.2 eV and the corresponding integrated angular distributions are given in Fig. S10(c) and (d).† As seen, the similar scattering signatures to $TaCH_2^+$ are observed for $TaCD_2^+$, suggesting that the $Ta^+ + CD_4$ reaction is also controlled by the indirect mechanism. The distribution of the internal energy, as shown in Fig. S10(e) and (f),† in the $Ta^+ + CD_4$ reaction is also very similar to the one in the $Ta^+ + CH_4$ reaction.

Conclusions

To summarize, the first set of full-dimensional PESs for the quintet, triplet, and singlet states of the $Ta^+ + CH_4 \rightarrow TaCH_2^+ + H_2$ reaction were developed at the B3LYP/DZ level based on PIP-

NN fits of 64 300 points. Multi-state nonadiabatic dynamical calculations were performed on these PESs using the FSSH method, with spin–orbital couplings (SOCs) determined from MRCI calculations. The calculated thermal rate coefficients are found to be in good agreement with the newly acquired experimental data in the temperature range between 300 and 600 K. However, this good agreement was only achieved after ZPE correction based on the 1GB scheme. The significant ZPE violation can be attributed to the near thermoneutrality of the reaction, and the large vibrational frequency of the H_2 product. Additionally, the intersystem crossing between the quintet and triplet states, rather than the triplet saddle point, is the kinetic bottleneck of this reaction because of the very close proximity of the crossing point to the triplet saddle point.

The dynamical calculations predict product angular distributions consistent with the molecular beam measurements, although minor differences exist at relatively high collision energies. Our calculations support the experimental finding that the title reaction is predominantly governed by an indirect mechanism, even at higher collision energies. Additional evidence supporting this conclusion is that we found that there is no correlation between the scattering angle and the impact parameter as discussed above. More importantly, our analysis attributes the indirect mechanism to two long-lived reaction intermediates in the exit channel. Also consistent with the slow relative recoil velocity observed in the experiment, the internal DOFs of the $TaCH_2^+$ product are found to be excited. However, the energy disposal into the products was found to be equally partitioned into each individual degree-of-freedom, representing a statistical distribution, thanks to the long lifetime of the reaction intermediate, which allows efficient and complete energy randomization. The long lifetime also leads to the nonnegligible contribution of the singlet state to the reaction.

We emphasize that the DFT treatment of the electronic structure is an approximation, which ignores many important details such as spin–orbit coupling and multi-reference characteristics. Nevertheless, the reasonably good agreement with available experimental data supports the validity of the theoretical model used to describe the kinetics and dynamics of this prototypical model reaction for the activation of methane. It is clearly shown that the reaction is facilitated by a "spin-forbidden" mechanism, in which a barrierless pathway is in-turn facilitated by ISC from the quintet state to the triplet state, followed by mixing between the triplet and singlet states. This two-state reactivity mechanism is expected to be instructive in understanding the catalytic capacity of transition metals in more complex environments such as single atom catalysis.

Methods

Electronic structure calculations

The geometries, energies, and harmonic frequencies of all stationary points are calculated at the B3LYP/DZ level,[41,42] using the aug-cc-pVDZ basis set for C and H and the ECP60MD-F_AVDZ basis set for Ta.[43] This level of theory is also used to construct the quintet, triplet, and singlet PESs for the $Ta^+ + CH_4$ system. To prevent the B3LYP/DZ calculations from converging to electronically excited states, which can occur due to the numerous low-lying excited states in the $Ta^+ + CH_4$ system, the wave function stability analysis was performed before each calculation. This ensured that the ground electronic state for the relevant spin multiplicity was correctly retrieved. All DFT calculations were performed with the Gaussian quantum chemical program.[44]

The SOC calculations were performed at the multi-reference configurational interaction with the same basis set as in DFT (MRCI/DZ).[45,46] The complete active space self-consistent field (CASSCF) method[47,48] was used to provide the wave functions and reference states for subsequent MRCI calculations. The CASSCF calculations employed an active space of 6 electrons in 7 orbitals (6e, 7o), considering two singlet, two triplet, and two quintet molecular terms (18 states in total). We selected seven geometries near the quintet/triplet MECP from the minimum energy path (MEP) on the triplet state and performed the SOC calculations. For each point, the root-mean-square of the sum of the MRCI SOC matrix elements was used to provide an averaged value.[49] As shown in Fig. S11,† the SOC values of the seven points show no significant variation. The average value of these points was used for our dynamical calculations. MRCI calculations were performed using Molpro software,[50] and the MECP search was conducted with the EasyMECP program,[51] modified to allow for wave function stabilization prior to each DFT calculation.

Potential energy surfaces

To cover all relevant configuration spaces for the $Ta^+ + CH_4 \rightarrow TaCH_2^+ + H_2$ reaction, about 64 300 points were sampled and calculated the quintet, triplet, and singlet state energies at the B3LYP/DZ level. The PIP-NN method[52,53] was employed to fit these energy points in the full twelve dimensions. The NN input layer employs permutation-invariant polynomials (PIPs) to enforce the symmetry of the four identical hydrogen atoms. For the $Ta^+ + CH_4$ system, 1052 PIPs up to fifth order were employed in the NN input layer. The Morse-like variables $p_{ij} = \exp\left(\frac{-r_{ij}}{\lambda}\right)$ were used to construct the PIPs,[54] where r_{ij} represents the internuclear distance and λ is an adjustable constant set to 1.8 Å in this work. After several tests, a neural network structure of 1052-5-100 was chosen, which results in 5966 fitting parameters for each spin-specific PES. To prevent overfitting, the "early stopping" method was employed, which involved randomly splitting the dataset into 90% for training and 5% each for validation and testing. This strategy ensures that the model remains generalizable and effective across various data subsets. The fittings are accepted only when the RMSEs for the training, validation, and test sets were comparable, effectively preventing false extrapolation. The Levenberg–Marquardt algorithm was utilized for NN training.[55]

Since both H_2 and CH_4 have no dipole, very small quadrupoles, and small polarizability. No special treatment of the electrostatic interaction was applied in the long range. However, we have carefully checked the PIP-NN PESs near the asymptote and found them to be smooth and possess no artificial features as depicted in Fig. S12.†

Trajectory surface hopping

The dynamical calculations were performed using Tully's fewest switches surface hopping (FSSH) method.[56] This semiclassical treatment of nonadiabatic dynamics involves using classical mechanics to describe the nuclear motion on each electronic state PES, with the electronic motion governed by quantum mechanics. The FSSH algorithm determines the transition probability from one electronic state to another at each timestep, utilizing the electronic wavefunctions and nonadiabatic coupling elements. Then, a random number, drawn uniformly between 0 and 1, is used to compare against this probability to decide if a hop should take place. When a hop happens, the nuclear momenta are altered to ensure total energy conservation. In the FSSH calculations, the SOC values between the quintet and triplet, the quintet and singlet, and the triplet and singlet are 280.7, 0.0, and 192.6 cm^{-1}, respectively. The 2023 version of the ANT program[57] was employed to perform the FSSH calculations.

A trajectory is initiated with the reactants at an initial separation of 12 Å and terminated when the reactants or products reached the same separation distance. All trajectories start on the quintet reactant asymptote. The maximum impact parameter (b_{max}) is set to match the initial separation between the collision partners, ensuring it is large enough for convergence of the results. The impact parameter (b) is calculated using the equation $b = b_{max}\xi^{1/2}$, with ξ being a random number uniformly distributed between 0 and 1. For trajectory integration, the Bulirsch–Stoer method with adaptive step size was employed.

The thermal rate coefficients are calculated at the temperatures of 300, 400, 500, and 600 K. The translational, vibrational, and rotational degrees of freedom of the reactants were sampled using the Boltzmann distribution at the specified temperature. The dynamic calculations were performed at the experimental collision energies (E_c) of 0.7, 1.0, and 1.3 eV, with CH_4 in its ground ro-vibrational state. To keep the statistical error under 5.0%, 1.0×10^4 trajectories for thermal rate calculations and 2.0×10^5 trajectories were initiated for dynamical calculations. Almost all trajectories maintain energy conservation within a 10^{-3} eV criterion.

The following equation was used to calculate the reactive integral cross section (ICS) for the product channel $TaCH_2^+ + H_2$:

$$\sigma_r(E_c) = \pi {b_{max}}^2 P_r(E_c). \quad (1)$$

Here, the reaction probability $P_r(E_c)$ is expressed as the ratio of reactive trajectories (N_r) to the total number of trajectories (N_{total}) for a specified collision energy E_c. The statistical error was calculated by $\Delta = \sqrt{(N_{total} - N_r)/(N_{total}N_r)}$.

The differential cross section (DCS) is calculated using the following formula:

$$\frac{d\sigma_r}{d\Omega} = \frac{\sigma_r P_r(\theta)}{2\pi \sin(\theta)}, \quad (2)$$

where θ is the scattering angle, and Ω is the scattering solid angle.

The following experimental definition of the scattering angle[37] was used:

$$\theta = 180^\circ - \cos^{-1}\left(\frac{\vec{v}_i \cdot \vec{v}_f}{|\vec{v}_i||\vec{v}_f|}\right), \quad (3)$$

where v_i represents the initial velocity vector of Ta^+ ion and v_f represents the final velocity vector of $TaCH_2^+$. Therefore, in this definition, forward scattering ($\theta = 0^\circ$) means a direct rebound of the $TaCH_2^+$ product, whereas backward scatter ($\theta = 180^\circ$) means the $TaCH_2^+$ product moves in the same direction as the original Ta^+ reactant.

The following formula was used to calculate the thermal rate coefficient:

$$k = g_e(T)\sqrt{\frac{8k_BT}{\pi\mu_R}}\pi {b_{max}}^2 \frac{N_r}{N_{total}}, \quad (4)$$

where k_B represents the Boltzmann constant, μ_R denotes the reactant reduced mass, and $g_e(T)$ is the electronic degeneracy factor of the quintet state:

$$g_e(T) = \frac{Q_{TaCH_4^+}}{Q_{Ta^+}Q_{CH_4}} = \frac{5}{3 + 5e^{-1483.9K/T} + 7e^{-3801.5K/T} + 9e^{-6353.2K/T} + 11e^{-8901.4K/T}}, \quad (5)$$

where the energies in the determinator correspond to the experimental energy levels of spin–orbit states of the Ta^+ (^5F) cation.[5]

In quasi-classical trajectory simulations, molecular vibrations are not quantized, and the vibrational energy is allowed to fall below ZPE. To address the ZPE leakage issue, trajectories that violate ZPE can be removed, a technique known as hard-ZPE correction. A more reasonable approach is the Gaussian binning (GB) method,[58] which incorporates quantum effects into the quasi-classical results by assigning a weight to each reactive trajectory. However, as the number of vibrational modes increases, the computational cost of GB grows exponentially, making it unsuitable for polyatomic products. To address this problem, Czakó and Bowman proposed the 1GB method,[59] in which the following Gaussian weight is attached to each trajectory:

$$G(n) = \frac{\exp\left[\left(\frac{E(n') - E(n)}{2E(0)}\right)^2 \Big/ \beta^2\right]}{\sqrt{\pi}\beta}, \quad (6)$$

where $E(n')$ is the exact classical vibrational energy obtained by using the final Cartesian coordinates and velocities and $E(n)$ is the harmonic vibrational energy at state n. $E(0)$ is the harmonic ZPE. $\beta = \delta/(2\sqrt{\ln 2})$, where δ is the full width at half maximum, set to 0.5 in this work after the testing. The weight for the corresponding vibrational states of the two products ($TaCH_2^+$ and H_2) is calculated as the product of two Gaussians, $G(n) = G(n_1,n_2,n_3,n_4,n_5,n_6) \times G(n_7)$.

The reaction probability is calculated using the following formula, as suggested by Bonnet and Espinosa-García:[60]

$$P_{1GB} = \frac{\sum_i^{N_r} G_i(n)}{\sum_i^{N_r} G_i(n) + \sum_k^{N_T - N_r} G'_k(m)}, \quad (7)$$

where N_r and N_T are the number of reactive and total trajectories, respectively. m represent the vibrational states of CH_4 in the nonreactive trajectories. In eqn (7), the denominator encompasses the sum of all computed trajectories, reactive and non-reactive.

SIFT

Thermal rate constants were measured using a selected-ion flow tube apparatus, similar to described elsewhere.[61] Briefly, Ta^+ ions were formed using a laser vaporization source *via* impinging the second harmonic of an Nd:YAG laser operating at 100 Hz onto a rotating, translating tantalum rod (ESPI metals, 99.9%). Ions were entrained into an expansion of argon (99.999%, Matheson) through a pulsed valve (Iota One) with an 0.2 mm aperture also operating at 100 Hz. Ions were mass-selected using a quadrupole mass filter and transported *via* a series of quadrupole ion guides to the entrance of a 7 cm diameter, 1 m long, stainless steel flow tube and injected against a pressure gradient *via* a Venturi inlet into a 10^2 m s^{-1} flow of helium (99.999%, Matheson). 59 cm prior to the terminus of the flow tube, reactant gas (methane, AirGas 99.99%) was added using a mass flow controller (MKS) *via* a 1/8″ diameter finger inlet. At the terminus of the flow tube, the core of the flow was sampled *via* a 3 mm aperture in a rounded, carbon-coated nosecone. Ions entered a higher vacuum region and were transported using a quadrupole ion guide to the entrance of an orthogonally-accelerated reflectron time-of-flight mass spectrometer. Relative reactant and product ion concentrations were monitored as a function of methane concentration in the flow tube. Rate constants were derived in the standard manner assuming pseudo-first order kinetics.

Only the rate constants for decay of the primary Ta^+ ion are reported here, with discussion of the significant sequential chemistry reserved for a later publication.

Data availability

The data supporting this article have been included as part of the ESI.†

Author contributions

The manuscript was written by Y. L. and H. G. with contributions of all authors. All authors have given approval to the final version of the manuscript. M. O., S. G. A., N. S. S., J. M. and H. G designed the project. Y. L. and M. O performed the calculations. T. W. R. L., S. G. A. and N. S. S. performed the SIFT experiments. All authors participated in the data analysis. H. G. directed the project.

Conflicts of interest

There are no conflicts of interest to declare.

Acknowledgements

This work at UNM was supported by Air Force Office of Scientific Research (FA9550-22-1-0350 to H. G.). Support for AFRL authors was provided by the Air Force Office of Scientific Research under AFOSR-22RVCOR009. J. M. acknowledges support by the Deutsche Forschungsgemeinschaft DFG (Project number 500279291). The computation was performed at CARC (Center for Advanced Research Computing) at UNM and at the HPC infrastructure LEO of the University of Innsbruck. The views expressed are those of the authors and do not reflect the official guidance or position of the Department of the Air Force, the Department of Defense (DoD), or the U.S. government.

References

1 J. A. Labinger and J. E. Bercaw, *Nature*, 2002, **417**, 507–514.
2 R. Horn and R. Schlögl, *Catal. Lett.*, 2015, **145**, 23–39.
3 A. A. Latimer, H. Aljama, A. Kakekhani, J. S. Yoo, A. Kulkarni, C. Tsai, M. Garcia-Melchor, F. Abild-Pedersen and J. K. Nørskov, *Phys. Chem. Chem. Phys.*, 2017, **19**, 3575–3581.
4 D. R. Lide, *CRC Handbook of Chemistry and Physics*, CRC Press, Boca Raton, FL, 2005.
5 A. Kramida, Y. Ralchenko, J. Reader and NIST ASD Team, *NIST Atomic Spectra Database (version 5.12)*, 2024, **https://physics.nist.gov/asd**.
6 J. Wei and E. Iglesia, *J. Catal.*, 2004, **224**, 370–383.
7 Z. Liu, D. C. Grinter, P. G. Lustemberg, T.-D. Nguyen-Phan, Y. Zhou, S. Luo, I. Waluyo, E. J. Crumlin, D. J. Stacchiola, J. Zhou, J. Carrasco, H. F. Busnengo, M. V. Ganduglia-Pirovano, S. D. Senanayake and J. A. Rodriguez, *Angew. Chem., Int. Ed.*, 2016, **55**, 7455–7459.
8 P. G. Lustemberg, R. M. Palomino, R. A. Gutiérrez, D. C. Grinter, M. Vorokhta, Z. Liu, P. J. Ramírez, V. Matolín, M. V. Ganduglia-Pirovano, S. D. Senanayake and J. A. Rodriguez, *J. Am. Chem. Soc.*, 2018, **140**, 7681–7687.
9 Z. Zuo, S. Liu, Z. Wang, C. Liu, W. Huang, J. Huang and P. Liu, *ACS Catal.*, 2018, **8**, 9821–9835.
10 M. Akri, S. Zhao, X. Li, K. Zang, A. F. Lee, M. A. Isaacs, W. Xi, Y. Gangarajula, J. Luo, Y. Ren, Y.-T. Cui, L. Li, Y. Su, X. Pan, W. Wen, Y. Pan, K. Wilson, L. Li, B. Qiao, H. Ishii, Y.-F. Liao, A. Wang, X. Wang and T. Zhang, *Nat. Commun.*, 2019, **10**, 5181.
11 Y. Tang, Y. Wei, Z. Wang, S. Zhang, Y. Li, L. Nguyen, Y. Li, Y. Zhou, W. Shen, F. F. Tao and P. Hu, *J. Am. Chem. Soc.*, 2019, **141**, 7283–7293.
12 D. K. Böhme and H. Schwarz, *Angew. Chem., Int. Ed.*, 2005, **44**, 2336–2354.
13 S. M. Lang and T. M. Bernhardt, *Phys. Chem. Chem. Phys.*, 2012, **14**, 9255–9269.
14 H. Schwarz, *Catal. Sci. Techno.*, 2017, **7**, 4302–4314.
15 S. W. Buckner, T. J. MacMahon, G. D. Byrd and B. S. Freiser, *Inorg. Chem.*, 1989, **28**, 3511–3518.
16 K. K. Irikura and J. Beauchamp, *J. Phys. Chem.*, 1991, **95**, 8344–8351.
17 J. C. Weisshaar, *Acc. Chem. Res.*, 1993, **26**, 213–219.
18 R. B. Metz, *Int. Rev. Phys. Chem.*, 2004, **23**, 79–108.

19 J. Roithová and D. Schröder, *Chem. Rev.*, 2010, **110**, 1170–1211.
20 H. Schwarz, *Angew. Chem., Int. Ed.*, 2011, **50**, 10096–10115.
21 H. Schwarz, *J. Chem.*, 2014, **54**, 1413–1431.
22 K. K. Irikura and J. L. Beauchamp, *J. Am. Chem. Soc.*, 1991, **113**, 2769–2770.
23 M. Pavlov, M. R. A. Blomberg, P. E. M. Siegbahn, R. Wesendrup, C. Heinemann and H. Schwarz, *J. Phys. Chem. A*, 1997, **101**, 1567–1579.
24 X.-G. Zhang, R. Liyanage and P. B. Armentrout, *J. Am. Chem. Soc.*, 2001, **123**, 5563–5575.
25 M. M. Armentrout, F.-X. Li and P. B. Armentrout, *J. Phys. Chem. A*, 2004, **108**, 9660–9672.
26 P. B. Armentrout, S. Shin and R. Liyanage, *J. Phys. Chem. A*, 2006, **110**, 1242–1260.
27 F.-X. Li, X.-G. Zhang and P. B. Armentrout, *Int. J. Mass Spectrom.*, 2006, **255–256**, 279–300.
28 L. G. Parke, C. S. Hinton and P. B. Armentrout, *J. Phys. Chem. C*, 2007, **111**, 17773–17787.
29 A. Shayesteh, V. V. Lavrov, G. K. Koyanagi and D. K. Bohme, *J. Phys. Chem. A*, 2009, **113**, 5602–5611.
30 J. F. Eckhard, T. Masubuchi, M. Tschurl, R. N. Barnett, U. Landman and U. Heiz, *J. Phys. Chem. A*, 2021, **125**, 5289–5302.
31 P. B. Armentrout, L. Parke, C. Hinton and M. Citir, *ChemPlusChem*, 2013, **78**, 1157–1173.
32 B. Ruscic, R. E. Pinzon, M. L. Morton, G. von Laszevski, S. J. Bittner, S. G. Nijsure, K. A. Amin, M. Minkoff and A. F. Wagner, *J. Phys. Chem. A*, 2004, **108**, 9979–9997.
33 B. Ruscic, R. E. Pinzon, G. von Laszewski, D. Kodeboyina, A. Burcat, D. Leahy, K. A. Amin, M. Minkoff and A. F. Wagner, *J. Phys.: Conf. Ser.*, 2005, **16**, 561.
34 P. B. Armentrout, *Science*, 1991, **251**, 175–179.
35 D. Schröder, S. Shaik and H. Schwarz, *Acc. Chem. Res.*, 2000, **33**, 139–145.
36 H. Schwarz, *Int. J. Mass Spectrom.*, 2004, **237**, 75–105.
37 M. Meta, M. E. Huber, M. Birk, M. Wedele, M. Ončák and J. Meyer, *Faraday Discuss.*, 2024, **251**, 587–603.
38 Y. Liu, M. Ončák, J. Meyer, S. G. Ard, N. S. Shuman, A. A. Viggiano and H. Guo, *J. Am. Chem. Soc.*, 2024, **146**, 14182–14193.
39 Y. Liu, M. Ončák, J. Meyer, S. G. Ard, N. S. Shuman, A. A. Viggiano and H. Guo, *J. Phys. Chem. A*, 2024, **128**, 6943–6953.
40 S. Essafi, D. P. Tew and J. N. Harvey, *Angew. Chem., Int. Ed.*, 2017, **56**, 5790–5794.
41 A. D. Becke, *J. Chem. Phys.*, 1993, **98**, 5648–5652.
42 C. Lee, W. Yang and R. G. Parr, *Phys. Rev. B:Condens. Matter Mater. Phys.*, 1988, **37**, 785–789.
43 K. A. Peterson, D. Figgen, M. Dolg and H. Stoll, *J. Chem. Phys.*, 2007, **126**, 124101.
44 M. J. Frisch, G. W. Trucks, H. B. Schlegel, G. E. Scuseria, M. A. Robb, J. R. Cheeseman, G. Scalmani, V. Barone, G. A. Petersson, H. Nakatsuji, X. Li, M. Caricato, A. V. Marenich, J. Bloino, B. G. Janesko, R. Gomperts, B. Mennucci, H. P. Hratchian, J. V. Ortiz, A. F. Izmaylov, J. L. Sonnenberg, D. Williams-Young, F. Ding, F. Lipparini, F. Egidi, J. Goings, B. Peng, A. Petrone, T. Henderson, D. Ranasinghe, V. G. Zakrzewski, J. Gao, N. Rega, G. Zheng, W. Liang, M. Hada, M. Ehara, K. Toyota, R. Fukuda, J. Hasegawa, M. Ishida, T. Nakajima, Y. Honda, O. Kitao, H. Nakai, T. Vreven, K. Throssell, J. A. Montgomery Jr, J. E. Peralta, F. Ogliaro, M. J. Bearpark, J. J. Heyd, E. N. Brothers, K. N. Kudin, V. N. Staroverov, T. A. Keith, R. Kobayashi, J. Normand, K. Raghavachari, A. P. Rendell, J. C. Burant, S. S. Iyengar, J. Tomasi, M. Cossi, J. M. Millam, M. Klene, C. Adamo, R. Cammi, J. W. Ochterski, R. L. Martin, K. Morokuma, O. Farkas, J. B. Foresman and D. J. Fox, *Gaussian 16, Revision C.01*, Gaussian Inc., Wallingford, CT, 2016.
45 H.-J. Werner and P. J. Knowles, *J. Chem. Phys.*, 1988, **89**, 5803–5814.
46 P. J. Knowles and H.-J. Werner, *Chem. Phys. Lett.*, 1988, **145**, 514–522.
47 B. O. Roos, P. R. Taylor and P. E. M. Siegbahn, *Chem. Phys.*, 1980, **48**, 157–173.
48 P. E. M. Siegbahn, J. Almlöf, A. Heiberg and B. O. Roos, *J. Chem. Phys.*, 1981, **74**, 2384–2396.
49 D. Danovich and S. Shaik, *J. Am. Chem. Soc.*, 1997, **119**, 1773–1786.
50 H. J. Werner, P. J. Knowles, G. Knizia, F. R. Manby and M. Schütz, *Wiley Interdiscip. Rev.: Comput. Mol. Sci.*, 2012, **2**, 242–253.
51 J. Rodríguez-Guerra, I. Funes-Ardoiz and F. Maseras, *EasyMECP. Zenodo, version v0.3.2*, 2018.
52 B. Jiang and H. Guo, *J. Chem. Phys.*, 2013, **139**, 054112.
53 J. Li, B. Jiang and H. Guo, *J. Chem. Phys.*, 2013, **139**, 204103.
54 B. J. Braams and J. M. Bowman, *Int. Rev. Phys. Chem.*, 2009, **28**, 577–606.
55 M. T. Hagan and M. B. Menhaj, *IEEE Trans. Neural Network.*, 1994, **5**, 989–993.
56 J. C. Tully, *J. Chem. Phys.*, 1990, **93**, 1061–1071.
57 Y. Shu, L. Zhang, J. Zheng, Z. H. Li, A. W. Jasper, D. A. Bonhommeau, R. Valero, R. Meana-Pañeda, S. L. Mielke, Z. Varga and D. G. Truhlar, *ANT 2023.B: A Program for Adiabatic and Nonadiabatic Trajectories, version v2; Zenodo*, 2023.
58 L. Bonnet and J.-C. Rayez, *Chem. Phys. Lett.*, 2004, **397**, 106–109.
59 G. Czakó and J. M. Bowman, *J. Chem. Phys.*, 2009, **131**, 244302.
60 L. Bonnet and J. Espinosa-Garcia, *J. Chem. Phys.*, 2010, **133**, 164108.
61 M. E. Huber, T. W. R. Lewis, M. Meta, S. G. Ard, Y. Liu, B. C. Sweeny, H. Guo, M. Ončák, N. S. Shuman and J. Meyer, *Phys. Chem. Chem. Phys.*, 2024, **26**, 8670–8680.